

Real-space microscopic description of laser-pulse induced melting of superconductivity

Karl Bergson Hallberg and Jacob Linder

Center for Quantum Spintronics, Department of Physics, Norwegian University of Science and Technology, NO-7491 Trondheim, Norway

Guillermo Nava Antonio

Cavendish Laboratory, University of Cambridge, CB3 0HE Cambridge, UK

Chiara Ciccarelli

Cavendish Laboratory, University of Cambridge, CB3 0HE Cambridge, UK and Center for Quantum Spintronics, Department of Physics, Norwegian University of Science and Technology, NO-7491 Trondheim, Norway

(Dated: March 19, 2026)

Quenching quantum order via laser pulses has proven a useful tool to access exotic physical effects in systems that are strongly perturbed out of equilibrium. However, theoretical modelling of experimental measurements is typically done phenomenologically or by assuming translational invariance due to the complexity of the problem. Here, we solve a microscopic real-space model of the time dynamics of a superconductor following an intense laser-pulse. We are able to reproduce recent experimental findings displaying a critical slowing-down of the melting of the order parameter for laser fluences close to the condensation energy. Moreover, we leverage the real-space resolution of our model to predict how phase fluctuations and currents in the system behave both spatially and temporally. We discover an unusual current flow in the superconductor after the pulse has subsided, resembling backward waves that normally require special engineering in metamaterials or wave guides. Our results predict a rich behavior of the superconducting order parameter at a microscopic level which is manifested in current textures that can be probed using radiation detection.

Introduction. Ultrafast optical pump-probe experiments have made it possible to observe superconductivity melting and recovering on timescales on the order of picoseconds [1–4]. These experiments allow one to visualize the melting and subsequent recovery of superconductivity revealing complex dynamics and non-monotonic behavior with regards to pump fluence [5–7]. The measurements probe a regime far out of equilibrium where a complex interplay of the various degrees of freedom determines observable phenomena such as melting and recovery times [8, 9].

Despite the experimental studies, a fully microscopic theoretical description capable of connecting the microscopic pairing physics to the experimentally accessible signals under strong time-dependent fields is lacking, in particular including spatial resolution of the dynamic superconducting order parameter. Phenomenological models such as Ginzburg-Landau give less intuition about the microscopic degrees of freedom and are not formally applicable far out of equilibrium and other models often work under the assumption of translational invariance or the electromagnetic field having a frequency less than that of the superconducting gap which is insufficient to completely destroy superconductivity [10–15].

In this Letter, we develop a microscopic, spatially-resolved, real-time and real-space description of the pump induced suppression and recovery of superconductivity on a 2D lattice. We investigate the dynamics of a superconductor subjected to a high-frequency laser pulse using self-consistent time-dependent Bogoliubov-de Gennes (BdG) equations and the Heisenberg equations within a tight-binding framework. This method allows for a spatially resolved treatment of the order parameter and the inclusion of the electromagnetic field via

the Peierl’s substitution modifying the hopping parameter, and thus opens the possibility to study ultrafast dynamics in heterostructures. Our microscopic model is able to reproduce the experimental observation [16] of a critical slowing-down of the superconducting melting for laser fluences close to the condensation energy. Moreover, from the real-space resolution of our simulations, we discover that the temporal and spatial phase fluctuations in the system produce an unusual current flow pattern in the superconductor after the duration of the laser pulse. The current flow has opposite phase and group velocity and is thus a physical realization of a backward wave [17] that normally requires special engineering of metamaterials [18] or wave guides [19]. Our results thus uncover different and rich behavior of the superconducting order parameter at a microscopic level, which can be experimentally probed using radiation detection. *Theory.* The superconductor is modelled by the following mean-field Hamiltonian defined on a $N_x \times N_y$ lattice

$$\begin{aligned} \hat{H} &= \hat{H}_h + \hat{H}_\Delta + \hat{H}_{\text{ph}} + \hat{H}_{\text{e-ph}} + \hat{H}_\mu + H_0 \\ &= \sum_{ij\sigma} (c_{i\sigma}^\dagger t_{ij}^{\sigma\sigma'}(\tau) c_{j\sigma'} + \text{H.c.}) + \sum_i (\Delta_i c_{i\uparrow}^\dagger c_{i\downarrow}^\dagger + \Delta_i^* c_{i\downarrow} c_{i\uparrow}) \\ &\quad + \sum_i \omega_{\text{ph}} b_i^\dagger b_i + \gamma \sum_{i\sigma} c_{i\sigma}^\dagger (b_i^\dagger + b_i) c_{i\sigma} + \sum_i \mu_i n_i^f + H_0, \end{aligned} \quad (1)$$

where τ is time, $\Delta_i \equiv U \langle c_{i\downarrow} c_{i\uparrow} \rangle$ is the superconducting order parameter, ω_{ph} is the frequency of the phonons, γ the strength of the coupling between fermions and phonons, μ_i is an onsite chemical potential, $n_i^f \equiv \sum_\sigma c_{i\sigma}^\dagger c_{i\sigma}$ and $H_0 = \sum_i |\Delta_i|^2 / |U|$. We employ Peierl’s substitution which entails modifying the

hopping term to include a time-dependent phase, which for a laser pulse with a spatial wavelength much larger than the relevant size of the superconductor simplifies to

$$t_{ij}(\tau) = \begin{cases} -t\mathbb{I}, & j = i + y \\ -te^{iaA_x(\tau)}\mathbb{I}, & j = i + x, \end{cases} \quad (2)$$

where a is the lattice constant and the vector potential is given by

$$A(\tau) = \Theta(\tau)A_0 e^{-\frac{(\tau-\tau_p)^2}{2\sigma_p^2}} \sin \Omega_{pf} \tau x. \quad (3)$$

The parameters used for the simulation are $t = a = \hbar = 1$, $N_x, N_y \in \{100, 120\}$, $U = -1$, $\omega \in \{0, 0.3\}$, $\gamma \in \{0, 0.05\}$, $\mu \in \{0, 0.3\}$, $A_0 \in [1, 3]$, $\sigma_p = 0.25$, $\tau_p = 5\sigma_p$, $\Omega_{pf} = 9.44$. The last four parameters were chosen to correspond to experiment.

Time dynamics and initial conditions. To investigate the effect of the laser pulse on the superconducting order parameter we are interested in the time evolution of correlators of the system such as $\langle c_{i\downarrow}c_{i\uparrow} \rangle(\tau)$. These correlations are calculated via the Heisenberg equation,

$$i \frac{d}{d\tau} \hat{O}_H(\tau) = [\hat{O}_H(\tau), \hat{H}(\tau)], \quad (4)$$

which lead to a large set of coupled non-linear differential equations. The Heisenberg equations allows us to track the time dependency of all the relevant microscopic correlations at a lattice resolution. Even though the Hamiltonian *a priori* only includes nearest neighbor hopping and on-site superconducting pairing, the commutator of *e.g.* $c_{i\downarrow}c_{i\uparrow}$ and the hopping term yields time dynamics dependent on arbitrary off-diagonal correlations $c_{i\downarrow}c_{j\uparrow}$, $i \neq j$. To produce a reasonable set of initial conditions, we assume that the system before the laser pulse is in equilibrium such that we may perform a mean-field approximation on the phonons. The derivation and the full sets of equations of motion are given in the supplemental material [20].

Absorbed energy and melting time. A recent experiment [16] showed that the time dynamics of the order parameter Δ , and in particular its melting, was strongly dependent on the absorbed energy due to the injected laser fluence. A critical slowing down of the order parameter melting was observed when the absorbed energy equaled an amount that was larger than the condensation energy of the superconductor, but smaller than the energy required to completely melt the superconducting order, $\Delta \rightarrow 0$. To compare the energy that is absorbed by the superconductor as a result of the laser in our model, we calculate the internal energy $\langle \hat{H} \rangle(\tau)$ with vector potential $A(\tau) = 0$ during the time evolution. A is set to zero because we are interested in the energy that is absorbed by the superconductor and not the energy associated with the vector potential which will vanish when the pulse is over. In this way only the energy that is absorbed by the system after the pulse subsides is

accounted for [21]. The internal energy is therefore given by

$$\begin{aligned} \langle \hat{H}[A=0] \rangle &= \sum_{ij} \text{tr}(t_{ij}^s \rho_{ij}) + \sum_i \left(\Delta_i \Gamma_{ii}^{\uparrow\downarrow} + \Delta_i^* F_{ii}^{\downarrow\uparrow} \right) \\ &+ \sum_l \omega_{\text{ph}} \langle n_l^b \rangle + \sum_i (\gamma X_i + \mu_i) \langle n_i^f \rangle + H_0, \end{aligned} \quad (5)$$

where the trace is over the spin degrees of freedom.

We track the change in this value at time τ to its value at time $\tau = 0$, i.e. the change in, or absorbed, internal energy

$$\mathcal{E}(\tau) \equiv \langle \hat{H}[A=0] \rangle(\tau) - \langle \hat{H}[A=0] \rangle(0). \quad (6)$$

This value may in turn be compared to the difference in internal energy between the superconducting state and normal state in equilibrium before the pulse is turned on,

$$\mathcal{E}_{\text{sc}} \equiv |\langle \hat{H} \rangle_{\text{sc}}(0) - \langle \hat{H} \rangle_{\text{n}}(0)|, \quad (7)$$

which provides a sense of scale of the energy absorbed from the laser pulse. After the pulse is turned on, the system is no longer in equilibrium, therefore we do not have access to equilibrium values such as temperature, and we cannot meaningfully calculate values such as the free energy. Therefore we find that it is more meaningful to compare the change in internal energy to the difference in internal energy between the superconducting state and the normal state before the quench, and not the condensation energy given by the difference in free energy between the superconducting and normal state. This is because the free energy also includes a contribution from entropy S . However, at very low temperatures T , the condensation energy and internal energy difference at equilibrium coincide since $TS \rightarrow 0$. As for the melting time τ_m , it is defined as the time it takes for the site-averaged order parameter to reach within a percentage of its minimum value, in this Letter we have used 1%. This is to reduce the influence of numerical inaccuracies and small oscillations, especially in cases where the order parameter changes very little from its original value.

Results. We start by considering the case without phonons. The temperature dependence of τ_m is shown in Fig. 1. Here the melting time at each temperature is plotted versus the total absorbed energy after the laser pulse has subsided. Although the absolute value of the absorbed energy is different for each temperature, the qualitative behavior is similar in that the maximum of τ_m always occurs for an absorbed energy between \mathcal{E}_{sc} and \mathcal{E}_d , which is defined as the energy where the order parameter reaches zero at some point during the time evolution. The black dots mark the values where $\mathcal{E}_f = \mathcal{E}_{\text{sc}}$ for each temperature, and the red dots mark the values where $\mathcal{E}_f = \mathcal{E}_d$ respectively. The superconductivity is destroyed completely for all temperatures shortly after the peak value of τ_m . This is in agreement with the recent experiment Ref. [16]. Our model does not include any specific dissipation mechanism, which means that the system should persist in a non-equilibrium state. However, that does not mean that the order parameter cannot reach a stationary value [22]. For instance, oscillatory behavior of the order parameter can be lost for large times despite the lack

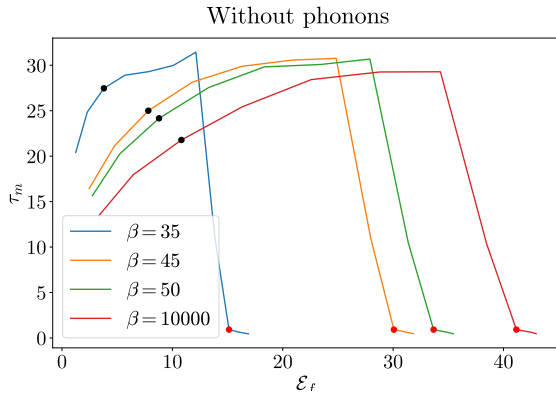


FIG. 1. Melting time τ_m versus absorbed internal energy for different choices of inverse temperature $\beta = 1/T$. The black dots mark the melting time at the absorbed energy which equals the difference in internal energy of the superconducting and normal state at time zero, \mathcal{E}_{sc} . The red dots mark the melting time at the absorbed energy where the average of the order parameter goes to zero at some point during the time evolution. Parameters used are $N_x = 100$ and $\omega = \gamma = 0$.

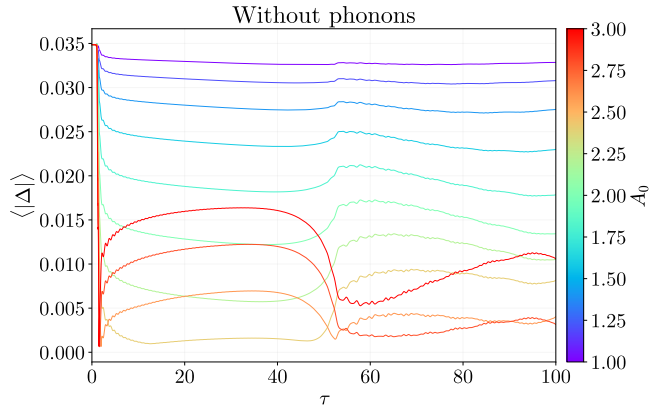


FIG. 2. Several time evolutions of the order parameter averaged over sites at inverse temperature $\beta = 35$ with different choices of the parameter A_0 varying between 1 – 3. Parameters used are $N_x = 100$ and $\omega = \gamma = 0$.

of dissipation in the system due to so-called quench-induced decoherence [23]. In effect, we are assuming that dissipation mechanisms of energy, such as heat loss to the environment, occur at longer time scales than the τ -values considered in Fig. 2. The plot shows that the order parameter is gradually suppressed with increasing A_0 , until it finally changes sign around $A_0 \simeq 2.5$. This causes the absolute value to recover abruptly and results in a sharp reduction in melting time since the minimum value of Δ turns into a local maximum of $|\Delta|$ as Δ changes sign. The laser pulse thus causes an "overshoot" of the suppression of the order parameter beyond zero into negative values, whereas the U(1) symmetry of the superconducting condensate after the laser pulse has subsided renders $|\Delta|$ the physically meaningful quantity.

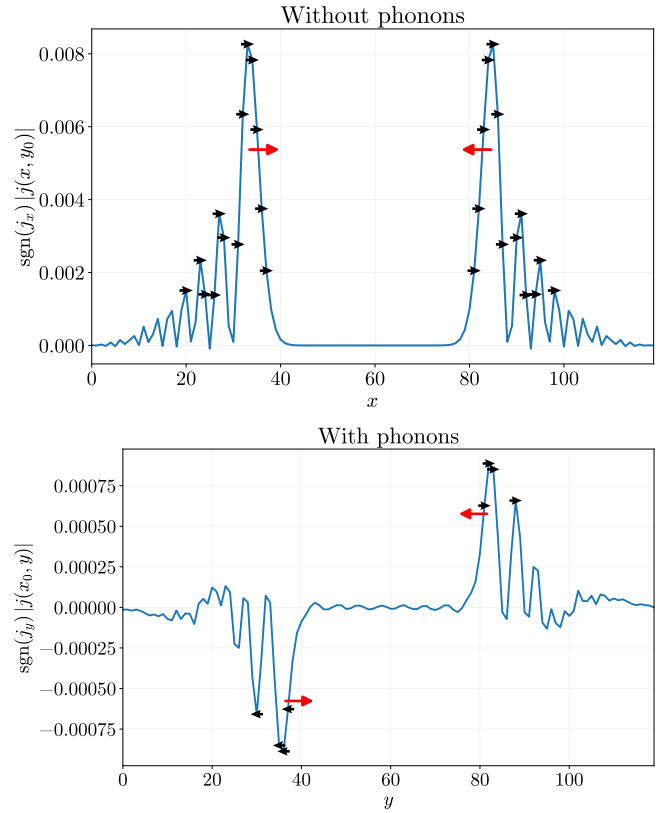


FIG. 3. Direction and signed magnitude of currents of a slice of the superconductor at $\tau = 20$. The upper plot shows a slice $y_0 = 60$ for a superconductor without phonons. Both wavefronts are moving towards each other and the other end of the lattice as indicated by the red arrows, however the current is all in the $+x$ -direction as indicated by the black arrows. The lower plot shows a slice $x_0 = 60$ for a superconductor with phonons. Both wavefronts are moving towards each other but in this case the direction of the current is opposite that of the wavefront for both ends. Parameters used are $N_x = 120$, $A_0 = 2.2$, $\beta = 10000$ for both, and $\gamma = 0.05$, $\omega = 0.3$ for the case with phonons.

The laser pulse induces transient bond-currents

$$\dot{j}_{i,i+\hat{e}} = -2\mathcal{J}\text{m}[\text{tr}(t_{i,i+\hat{e}} \rho_{i,i+\hat{e}})], \quad (8)$$

in the lattice, and spatial variations in the phase of the order parameters, ϕ_i . At low fluences, the magnitude of the current is approximately constant as a function of A_0 , and the spatial variation of the phase is small. However, after a critical value of A_0 is exceeded, corresponding to the energy \mathcal{E}_f required to completely drive the order parameter to zero, the pulse induces strong spatial variations in the phase, and the magnitude of the currents increases rapidly. The flow pattern of the currents is shown in Fig. 3 and consists of one magnitude-wavefront of $+x$ -direction currents traveling from $x = 0$ towards $x = N_x$, and one front of $+x$ -direction currents traveling the opposite way from $x = N_x$ to $x = 0$, where the direction is chosen by the wavevector of the vector potential. The wavefronts move with a speed of a little less than two lattice-sites per τ (in units of t), consistent with the dispersion-relation of a 2D

tight-binding model. This leads to an inherent time-scale of the system, which is the time needed for the two wavefronts to travel across the lattice and reflect on the boundary, flipping the sign of the currents. This event can be seen in the spatial variation of the phases ϕ_i , where the gradient of the phase switches sign at $\tau \approx N_x/2$, see Fig. 4. To understand why this is the case, imagine the laser pulse shifting the distribution of electrons equally across the whole lattice back and forth in the $\pm x$ -direction during the pulse. After the pulse subsides, one of the edges has a surplus of electrons whilst the other one has a deficit, and the middle of the lattice has shifted equally and hence has neither surplus nor deficit. The edge with the deficit refills with electrons, causing the current to move towards the left but leaving a deficit where the electrons were, which in turn causes the magnitude-front to move in the other direction as the distribution evens out. The opposite happens on the other side, where the surplus of electrons at the edge starts to spill out, causing a new surplus of electrons at the next site, which cascades into the current and magnitude-front moving in the same direction. On a finite lattice, this is caused by the hard boundary conditions. However, the hard boundary conditions are not necessary. The natural "boundaries" caused by a vector potential varying in space is also sufficient to cause regions with a surplus or deficiency of electrons. For example by assuming a laser pulse modulated by a Gaussian in the x - and y -directions on a lattice with periodic boundary conditions also creates current wavefronts with similar characteristics. More details are provided in the supplemental material [20]. Whereas pulse-induced currents have been discussed previously [24], this is to the best of our knowledge the first visualization of their actual flow pattern in real space. Moreover, we underline that the current excitation predicted in this work is different from a superfluid plasmon recently observed in [25], since such a plasmon relies on Coulomb interaction for its existence, which is not included in our model.

The spatial distribution of the phase has an additional effect, most notably in cases where the order parameter is nearly suppressed. In these situations, the phase loses coherence across the lattice which leads to further suppression of the order parameter. This may be seen in Fig. 5, where both $\langle |\Delta| \rangle \equiv 1/N \sum_i |\Delta_i|$ and $|\langle \Delta \rangle| \equiv |1/N \sum_i \Delta_i|$ are shown. When the coherence of the phases at different sites is lost, the phases on two different sites is essentially uncorrelated. When the order parameter is averaged over all sites, the random phases cancel out, leading to a reduction of the order parameter. Thus, we find that a laser-pulse of sufficient magnitude destroys superconductivity by means of inducing strong spatial phase fluctuations across the sample.

We proceed to determine how the quench-induced dynamics of the superconducting order parameter is altered when there exists a coupling between the superconducting electrons and an optical phonon mode ω . In this way, there can occur an energy exchange between the superconducting condensate and phonons in the system. Our self-consistent model thus captures both the extent to which phonons influence the melting of the superconducting state and how efficient the energy transfer

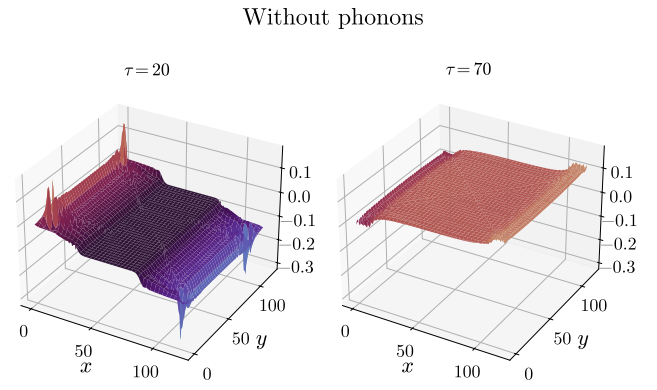


FIG. 4. Spatially resolved phase of the order parameters, $\arg(\Delta_i)$ at two different times, showing the correspondence between the gradient of the phase and the currents. Parameters used are $N_x = 120$, $A_0 = 2.2$, $\gamma = \omega = 0$ and $\beta = 10000$.

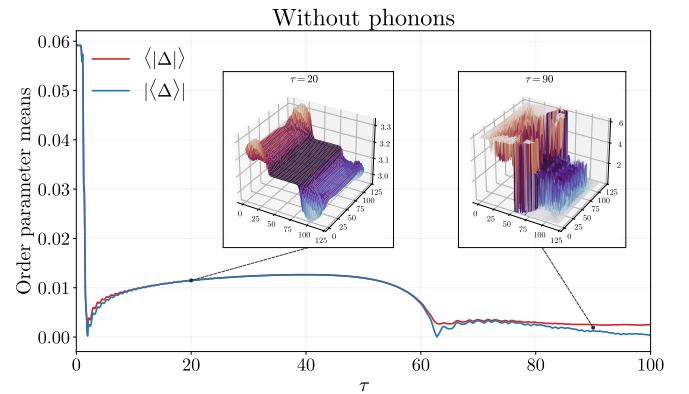


FIG. 5. Difference between $\langle |\Delta| \rangle$ and $|\langle \Delta \rangle|$, showing how coherence of phases between different lattice sites are lost after a reflection at the boundaries leading to a suppression of the order parameter. Parameters used are $N_x = 120$, $A_0 = 2.6$, $\gamma = \omega = 0$ and $\beta = 10000$.

between the superconducting condensate and the phonons is as a function of the injected energy through the laser quench. As pointed out in Ref. [26], acoustic phonons may play a key role in materials where optical phonon energies exceed 2Δ . Incorporation of such modes into the present framework may thus be an interesting future venue to explore.

The melting time and characteristics of the time evolution are detailed in the supplemental material (SM) [20], which includes videos of the spatially resolved order parameter and current time dynamics. With phonons or with a non-zero chemical potential, the time evolution renders the order parameter Δ to become fundamentally complex, as opposed to the mostly real Δ obtained in the time evolution without phonons, especially at low fluences. Specifically, the phonons induce a constantly rotating phase $|\Delta_i|e^{i(\phi_i + \omega\tau)}$ reminiscent of a Goldstone mode lingering after the pulse duration, in addition to a stronger spatial variation of the phase ϕ_i . Interestingly, the phonons modify the current flow in the superconductor. When the optical phonon mode is present, currents induced by small laser

fluences move not only in the x -direction but also feature a weak current with wavefronts travelling in the y -direction, as may be seen in Fig. 3. In fact, it follows analytically from our equations of motion that electron-phonon scattering physically has a very similar effect as a self-consistently determined spatially varying chemical potential [20], the latter also causing electron scattering as it mimicks the presence of disorder.

Concluding remarks. We have developed a microscopic real-space model of laser pulse-induced melting of superconductivity, demonstrating that it reproduces the experimentally observed critical slowing-down of the melting time near the condensation energy. This goes substantially beyond previously employed phenomenological theories, including the possibility to now treat ultrafast dynamics in heterostructures. Moreover, we reveal that strong pulses generate phase decoherence and backward-wave-like current textures with opposite phase and group velocity. This enables direct, experimentally testable links between absorbed energy, phase disorder, and current flow. Our findings are of relevance not only for nonequilibrium materials science, but also with respect to the usage of superconducting dynamics in terahertz technology.

Acknowledgments. K.B.H. and J. L. were supported by the Research Council of Norway through Grant No. 353894 and its Centres of Excellence funding scheme Grant No. 262633 “QuSpin.” Support from Sigma2 - the National Infrastructure for High Performance Computing and Data Storage in Norway, project NN9577K, is acknowledged.

-
- [1] C. Giannetti, M. Capone, D. Fausti, M. Fabrizio, F. Parmigiani, and D. Mihailovic, Ultrafast optical spectroscopy of strongly correlated materials and high-temperature superconductors: a non-equilibrium approach, *Advances in Physics* **65**, 58 (2016).
- [2] T. Kampfrath, K. Tanaka, and K. Nelson, Resonant and nonresonant control over matter and light by intense terahertz transients, *Nat. Photon.* **7**, 10.1038/nphoton.2013.184 (2013).
- [3] M. Koch, D. Mittleman, M. J. Ornik, and E. Castro-Camus, Terahertz time-domain spectroscopy, *Nat. Rev. Methods Prim.* **3**, 10.1038/s43586-023-00232-z (2023).
- [4] H. Nemeč, F. Kadlec, K. C., P. Kuzel, and P. Jungwirth, Ultrafast far-infrared dynamics probed by terahertz pulses: A frequency domain approach, *J. Chem. Phys.* **122**, 10.1063/1.1857851 (2005).
- [5] M. Beck, M. Klammer, S. Lang, P. Leiderer, V. V. Kabanov, G. N. Gol’tsman, and J. Demsar, Energy-gap dynamics of superconducting nbn thin films studied by time-resolved terahertz spectroscopy, *Phys. Rev. Lett.* **107**, 177007 (2011).
- [6] R. Matsunaga, Y. I. Hamada, K. Makise, Y. Uzawa, H. Terai, Z. Wang, and R. Shimano, Higgs amplitude mode in the bcs superconductors $\text{Nb}_{1-x}\text{Ti}_x\text{N}$ induced by terahertz pulse excitation, *Phys. Rev. Lett.* **111**, 057002 (2013).
- [7] M. Beck, I. Rousseau, M. Klammer, P. Leiderer, M. Mittendorf, S. Winnerl, M. Helm, G. N. Gol’tsman, and J. Demsar, Transient increase of the energy gap of superconducting nbn thin films excited by resonant narrow-band terahertz pulses, *Phys. Rev. Lett.* **110**, 267003 (2013).
- [8] R. Matsunaga and R. Shimano, Nonequilibrium bcs state dynamics induced by intense terahertz pulses in a superconducting nbn film, *Phys. Rev. Lett.* **109**, 187002 (2012).
- [9] V. V. Kabanov, J. Demsar, and D. Mihailovic, Kinetics of a superconductor excited with a femtosecond optical pulse, *Phys. Rev. Lett.* **95**, 147002 (2005).
- [10] T. Papenkort, V. M. Axt, and T. Kuhn, Coherent dynamics and pump-probe spectra of bcs superconductors, *Phys. Rev. B* **76**, 224522 (2007).
- [11] T. Papenkort, T. Kuhn, and V. Axt, Nonequilibrium dynamics and coherent control of bcs superconductors driven by ultrashort pulses, *J. Phys. Conf. Ser.* **193**, 012050 (2009).
- [12] M. Zachmann, M. D. Croitoru, A. Vagov, V. M. Axt, and T. Papenkort, Ultrafast terahertz-field-induced dynamics of superconducting bulk and quasi-1d samples, *New J. of Phys.* **15**, 055016 (2013).
- [13] T. Tanabe, K. Sugimoto, and Y. Ohta, Nonequilibrium dynamics in the pump-probe spectroscopy of excitonic insulators, *Phys. Rev. B* **98**, 235127 (2018).
- [14] P. C. Hohenberg and B. I. Halperin, Theory of dynamic critical phenomena, *Rev. Mod. Phys.* **49**, 435 (1977).
- [15] N. Goldenfeld, *Lectures on Phase Transitions and the Renormalization Group* (CRC Press, Boca Raton, 1992).
- [16] G. N. Antonio, T. Courtois, C. Pfaff, K. S. Shukla, A. Sudbø, S. Mangin, T. Hauet, and C. Ciccarelli, Real-time detection of critical slowing-down at the superconducting phase transition (2026), [arXiv:2603.12473](https://arxiv.org/abs/2603.12473) [cond-mat.supr-con].
- [17] A. H. Meitzler, Backward-wave transmission of stress pulses in elastic cylinders and plates, *The Journal of the Acoustical Society of America* **38**, 835–842 (1965).
- [18] J. S. Hummelt, S. M. Lewis, M. A. Shapiro, and R. J. Temkin, Design of a metamaterial-based backward-wave oscillator, *IEEE Transactions on Plasma Science* **42**, 930–936 (2014).
- [19] M. Ibanescu, S. G. Johnson, D. Roundy, C. Luo, Y. Fink, and J. D. Joannopoulos, Anomalous dispersion relations by symmetry breaking in axially uniform waveguides, *Phys. Rev. Lett.* **92**, 063903 (2004).
- [20] (See Supplemental Material for additional details on the derivation of the time-dependent equations of motion, gif-files showing videos of the phase- and current-dynamics, as well as additional plots).
- [21] T. Cui, X. Yang, C. Vaswani, J. Wang, R. M. Fernandes, and P. P. Orth, Impact of damping on the superconducting gap dynamics induced by intense terahertz pulses, *Phys. Rev. B* **100**, 054504 (2019).
- [22] F. Peronaci, M. Schiró, and M. Capone, Transient dynamics of d -wave superconductors after a sudden excitation, *Phys. Rev. Lett.* **115**, 257001 (2015).
- [23] M. Schiró and A. Mitra, Transient orthogonality catastrophe in a time-dependent nonequilibrium environment, *Phys. Rev. Lett.* **112**, 246401 (2014).
- [24] M. Puviani, R. Haenel, and D. Manske, Quench-drive spectroscopy and high-harmonic generation in bcs superconductors, *Phys. Rev. B* **107**, 094501 (2023).
- [25] A. von Hoegen, T. Tai, C. J. Allington, M. Yeung, J. Pettine, M. H. Michael, E. Viñas Boström, X. Cui, K. Torres, A. E. Kossak, B. Lee, G. S. D. Beach, G. D. Gu, A. Rubio, P. Kim, and N. Gedik, Imaging a terahertz superfluid plasmon in a two-dimensional superconductor, *Nature* **650**, 869–874 (2026).
- [26] J. Demsar, R. Averitt, A. J. Taylor, V. Kabanov, W. Kang, H. Kim, E. Choi, and S. Lee, Pair-breaking and superconducting state recovery dynamics in mg b_2 , *Physical review letters* **91**, 267002 (2003).

Supplemental Material

A. THEORY

A.1. Equations of motion

The minimal set of time derivatives necessary to produce a closed system of equations are, defining $\rho_{ij}^{\sigma\sigma'} \equiv \langle c_{i\sigma}^\dagger c_{j\sigma'} \rangle$, $\Gamma_{ij}^{\sigma\sigma'} \equiv \langle c_{i\sigma}^\dagger c_{j\sigma'}^\dagger \rangle$, $F_{ij}^{\sigma\sigma'} \equiv \langle c_{i\sigma} c_{j\sigma'} \rangle$, $X_i \equiv \langle b_i^\dagger + b_i \rangle$, $P_i \equiv \langle b_i - b_i^\dagger \rangle$, $n_i^b \equiv \langle b_i^\dagger b_i \rangle$,

$$\begin{aligned} i \frac{d}{d\tau} \rho_{ij}^{\sigma\sigma} = & \\ & \sum_k \left((t_{jk} + t_{kj}^*) \rho_{ik}^{\sigma\sigma} - (t_{ki} + t_{ik}^*) \rho_{kj}^{\sigma\sigma} \right) \\ & + \text{sgn } \sigma (\Delta_j \Gamma_{ij}^{\sigma\bar{\sigma}} - \Delta_i^* F_{ij}^{\bar{\sigma}\sigma}) \\ & + \gamma (X_j - X_i) \rho_{ij}^{\sigma\sigma} \\ & + (\mu_j - \mu_i) \rho_{ij}^{\sigma\sigma}, \end{aligned} \quad (1)$$

where

$$\text{sgn } \sigma = \begin{cases} +1, & \sigma = \uparrow \\ -1, & \sigma = \downarrow \end{cases} \quad (2)$$

$$\bar{\sigma} = \begin{cases} \downarrow, & \sigma = \uparrow \\ \uparrow, & \sigma = \downarrow \end{cases}. \quad (3)$$

Note that $F_{ij}^{\bar{\sigma}\sigma} = (\Gamma_{ji}^{\sigma\bar{\sigma}})^*$ and hence only one of F or Γ are required for the equations to close.

Similarly, for Γ , only $\Gamma^{\uparrow\downarrow}$ is required for the complete set,

$$\begin{aligned} i \frac{d}{d\tau} \Gamma_{ij}^{\uparrow\downarrow} = & \\ & - \sum_k \left((t_{ki} + t_{ik}^*) \Gamma_{kj}^{\uparrow\downarrow} + (t_{kj} + t_{jk}^*) \Gamma_{ik}^{\uparrow\downarrow} \right) \\ & + \Delta_j^* \rho_{ij}^{\uparrow\uparrow} - \Delta_i^* (\delta_{ij} - \rho_{ij}^{\downarrow\downarrow}) \\ & - \gamma (X_i + X_j) \Gamma_{ij}^{\uparrow\downarrow} \\ & - (\mu_i + \mu_j) \Gamma_{ij}^{\uparrow\downarrow}. \end{aligned} \quad (4)$$

For the phonon part, the equations of motion are given by

$$i \frac{d}{d\tau} X_i = \omega_{\text{ph}} P_i, \quad (5)$$

$$i \frac{d}{d\tau} P_i = \omega_{\text{ph}} X_i + 2\gamma \langle n_i^f \rangle, \quad (6)$$

$$i \frac{d}{d\tau} \langle n_i^b \rangle = -\gamma P_i \langle n_i^f \rangle, \quad (7)$$

where Eq. (7) is only needed for the purposes of calculating the internal energy.

A.2. Initial conditions

The laser pulse is turned on at time $t = 0$, after which the time dynamics is calculated according to the Heisenberg

equations for the various correlators of the system. In order to increase the numerical accuracy of the results, a precise set of initial conditions for the correlations are needed. This is accomplished by performing a mean-field approximation on the phonons under the assumption that before the laser pulse, the system is in equilibrium and at a very low temperature, hence using $b_i^\dagger b_i \rightarrow f^b(\omega_{\text{ph}})$, where f^b is the Bose-Einstein distribution, $b_i^\dagger + b_i \rightarrow X_i(0)$ and Eq.(6),

$$\begin{aligned} i \frac{d}{d\tau} P_i = 0 = \omega_{\text{ph}} X_i + 2\gamma \langle n_i \rangle \\ \implies X_i(-\infty) = -\frac{2\gamma}{\omega_{\text{ph}}} \langle n_i \rangle. \end{aligned} \quad (8)$$

This enables us to write the Hamiltonian in standard BdG form and find a reasonable self-consistent initial condition for the time evolution.

$$\begin{aligned} \hat{H}(-\infty) = & \\ & \sum_{ij\sigma} \frac{1}{2} (c_{i\sigma}^\dagger t_{ij} c_{j\sigma} - c_{i\sigma} t_{ji} c_{j\sigma}^\dagger) \\ & + \sum_i \frac{1}{2} [\Delta_i (c_{i\uparrow}^\dagger c_{i\downarrow}^\dagger - c_{i\downarrow}^\dagger c_{i\uparrow}^\dagger) + \Delta_i^* (c_{i\downarrow} c_{i\uparrow} - c_{i\uparrow} c_{i\downarrow})] \\ & + \sum_{i\sigma} \frac{1}{2} [c_{i\sigma}^\dagger (\mu_i + X_i(0)) c_{i\sigma} - c_{i\sigma} (\mu_i + X_i(0)) c_{i\sigma}^\dagger] \\ & + \sum_i \omega_{\text{ph}} f^b(\omega_{\text{ph}}). \end{aligned} \quad (9)$$

Introducing $\hat{c}_i \equiv (c_{i\uparrow}, c_{i\downarrow}, c_{i\uparrow}^\dagger, c_{i\downarrow}^\dagger)^T$ allows us to write the Hamiltonian in the form

$$\hat{H}(-\infty) = E_0 + \frac{1}{2} \sum_{ij} \hat{c}_i^\dagger \hat{H}_{ij} \hat{c}_j = E_0 + \frac{1}{2} \hat{c}^\dagger \hat{H} \hat{c}, \quad (10)$$

where $E_0 = \omega_{\text{ph}} N_{\text{ph}} f^b(\omega_{\text{ph}}) + \sum_i |\Delta_i|^2 / U$ and

$$\hat{H}_{ij} = \begin{pmatrix} (X_i(0) + \mu_i) \delta_{ij} + t_{ij} & \Delta_i (-i\sigma_y) \delta_{ij} \\ \Delta_i^* (i\sigma_y) \delta_{ij} & -(X_i(0) + \mu_i) \delta_{ij} - t_{ji} \end{pmatrix} \quad (11)$$

We solve the Hamiltonian self-consistently by making a guess for the values of Δ_i and $X_i(0)$ and diagonalize \hat{H} . The values for Δ_i and $X_i(0)$ on the next iteration are obtained from the eigenvectors $\check{\chi}_n$ with components $(\check{\chi}_n)_i = (u_{n,i\uparrow}, u_{n,i\downarrow}, v_{n,i\uparrow}, v_{n,i\downarrow})^T$ and the relations

$$c_{i\sigma} = \sum_{n>0} (u_{n,i\sigma} \gamma_n + v_{n,i\sigma}^* \gamma_n^\dagger) \quad (12)$$

$$\langle \gamma_n \gamma_m^\dagger \rangle = (1 - f(E_n)) \delta_{nm} \quad (13)$$

$$\langle \gamma_n^\dagger \gamma_m \rangle = f(E_n) \delta_{nm}, \quad (14)$$

yielding

$$\begin{aligned} \Delta_i = U \sum_{n>0} \left(u_{n,i\downarrow} (1 - f(E_n)) v_{n,i\uparrow}^* \right. \\ \left. + u_{n,i\uparrow} f(E_n) v_{n,i\downarrow}^* \right), \end{aligned} \quad (15)$$

and

$$\langle n_i \rangle = \sum_{\sigma, n > 0} \left(|u_{n, i\sigma}|^2 f(E_n) + |v_{n, i\sigma}|^2 (1 - f(E_n)) \right), \quad (16)$$

where $\sum_{n > 0}$ is short hand for $\sum_{\{n: E_n > 0\}}$ and f is the Fermi-Dirac distribution.

Once the Hamiltonian has converged to within an error margin, the correlations of the last iteration are used to serve as the initial condition for the time evolution via

$$\langle c_{i\downarrow} c_{j\uparrow} \rangle = \sum_{n > 0} \left(u_{n, i\downarrow} (1 - f(E_n)) v_{n, i\uparrow}^* + v_{n, i\downarrow}^* f(E_n) u_{n, j\uparrow} \right), \quad (17)$$

and

$$\langle c_{i\sigma}^\dagger c_{j\sigma} \rangle = u_{n, i\sigma}^* f(E_n) u_{n, j\sigma} + v_{n, i\sigma} (1 - f(E_n)) v_{n, j\sigma}^*. \quad (18)$$

A.3. Critical slowing down

The critical slowing of the time-dynamics as the order parameter approaches zero can also be illustrated heuristically using time-dependent Ginzburg-Landau (TDGL) theory as follows. For an order parameter ϕ with free-energy density

$$f(\phi) = \frac{a}{2} \phi^2 + \frac{b}{4} \phi^4, \quad (19)$$

where $b > 0$ and $a = a_0(T - T_c)$, the TDGL equation is given by, in the case of homogeneous order parameter,

$$\partial_\tau \phi = -\Gamma \frac{df}{d\phi} = -\Gamma(a\phi + b\phi^3), \quad (20)$$

where Γ is a kinetic coefficient of the order parameter [1, 2] Linearizing around a stationary solution, we can expand around $\phi(\tau) = \phi_0 + \delta\phi(\tau)$ giving,

$$\begin{aligned} f'(\phi_0 + \delta\phi) &= f'(\phi_0) + f''(\phi_0)\delta\phi + \mathcal{O}(\delta\phi^2) \\ &= f''(\phi_0)\delta\phi + \mathcal{O}(\delta\phi^2), \end{aligned} \quad (21)$$

since stationarity implies $f'(\phi_0) = 0$. This yields a linearized equation,

$$\partial_\tau(\delta\phi) = -\Gamma f''(\phi_0)\delta\phi. \quad (22)$$

The solution to this equation is given by

$$\delta\phi(\tau) = \delta\phi(0) e^{-\Gamma f''(\phi_0)\tau}, \quad (23)$$

with relaxation time $\tau_{\text{rel}} = (\Gamma f''(\phi_0))^{-1}$. The stationary solutions satisfy $f'(\phi_0) = 0$, giving

$$\phi_0(a + b\phi_0^2) = 0 \implies \phi_0 = \begin{cases} 0, & a > 0 \\ \pm\sqrt{-a/b}, & a < 0. \end{cases} \quad (24)$$

We use the free-energy density to evaluate the curvature as $T \rightarrow T_c$,

$$f''(\phi_0) = a + 3b\phi_0^2 = \begin{cases} a, & T > T_c \\ -2a, & T < T_c. \end{cases} \quad (25)$$

In both cases, $f''(\phi_0) \rightarrow 0$ as $T \rightarrow T_c$ and hence the relaxation time τ_{rel} diverges. Thus, as the stationary order parameter $\phi_0 \rightarrow 0$ when $T \rightarrow T_c$, the curvature $f''(\phi_0)$ vanishes and the decay time-scale grows, consistent with the increase of the melting time.

A.4. Doubled Hamiltonian

When the Hamiltonian does not contain any spin-mixing terms, *e.g.* just a straight hopping plus pairing Hamiltonian, the BdG Hamiltonian takes the form

$$\hat{H}_{ij} = \begin{pmatrix} t_{ij} & 0 & 0 & -\Delta_i \\ 0 & t_{ij} & \Delta_i & 0 \\ 0 & \Delta_i^* & -t_{ji} & 0 \\ -\Delta_i^* & 0 & 0 & -t_{ij} \end{pmatrix} \quad (26)$$

we can instead use the basis $(c_{i\uparrow}, c_{i\downarrow}^\dagger, c_{i\downarrow}, c_{i\uparrow}^\dagger)$ and rewrite it as

$$\hat{H}_{ij} = \begin{pmatrix} t_{ij} & \Delta_i & 0 & 0 \\ \Delta_i^* & -t_{ji} & 0 & 0 \\ 0 & 0 & t_{ij} & -\Delta_i \\ 0 & 0 & -\Delta_i^* & -t_{ji} \end{pmatrix} = \begin{pmatrix} \hat{H}_{ij}^+ & 0 \\ 0 & \hat{H}_{ij}^- \end{pmatrix}, \quad (27)$$

which means that the set of eigenvalues for the full matrix are given by $\{\pm E_1, \pm E_1, \pm E_2, \pm E_2, \dots, \pm E_N, \pm E_N\}$. This is proven as follows. Assume $(\zeta_n)_i = (u_{i\uparrow}, v_{i\downarrow})$ is an eigenvector of \hat{H}_{ij}^+ such that

$$\sum_j \begin{pmatrix} t_{ij} & \Delta_i \\ \Delta_i^* & -t_{ji} \end{pmatrix} \begin{pmatrix} u_{j\uparrow} \\ v_{j\downarrow} \end{pmatrix} = E_n \begin{pmatrix} u_{i\uparrow} \\ v_{i\downarrow} \end{pmatrix}. \quad (28)$$

Then

$$\sum_j t_{ij} u_{j\uparrow} + \Delta_i v_{i\downarrow} = E_n u_{i\uparrow} \quad (29)$$

$$-\Delta_i^* u_{i\uparrow} + \sum_j t_{ji} v_{j\downarrow} = E_n (-v_{i\downarrow}) \quad (30)$$

This is written compactly:

$$\sum_j \begin{pmatrix} t_{ij} & -\Delta_i \\ -\Delta_i^* & -t_{ji} \end{pmatrix} \begin{pmatrix} u_{j\uparrow} \\ -v_{j\downarrow} \end{pmatrix} = E_n \begin{pmatrix} u_{i\uparrow} \\ -v_{i\downarrow} \end{pmatrix}. \quad (31)$$

Hence, if $(u_{i\uparrow}, v_{i\downarrow})$ is an eigenvector of the upper block with eigenvalue E_n , then $(u_{i\uparrow}, -v_{i\downarrow})$ is an eigenvector of the lower block with the same eigenvalue E_n . In a similar way, we can show that if $(u_{i\uparrow}, v_{i\downarrow})$ is an eigenvector with eigenvalue E_n , then $(v_{i\downarrow}^*, u_{i\uparrow}^*)$ is an eigenvector of the second block with eigenvalue $-E_n$. There is also a second eigenvector of the upper block $(v_{i\downarrow}^*, -u_{i\uparrow}^*)$ with eigenvalue $-E_n$. In total we can

therefore find the components of four eigenvectors from the components of one.

Translated into the $4N$ case, we know that if there is an eigenvector $(u_{i\uparrow}, 0, 0, v_{i\downarrow})$ then there is one with the same eigenvalue given by $(0, u_{i\uparrow}, -v_{i\downarrow}, 0)$, one with negative eigenvalue at $(v_{i\downarrow}^*, 0, 0, -u_{i\uparrow}^*)$ and one with negative eigenvalue at $(0, v_{i\downarrow}^*, u_{i\uparrow}^*, 0)$. Note that this means that we can drop the spin indices.

Instead of working with the full $4N \times 4N$ matrix, we can thus work with the $2N \times 2N$ matrix \hat{H}^+ with components in the basis $(c_{i\uparrow}, c_{i\downarrow}^\dagger)$

$$\hat{H}_{ij}^+ = \begin{pmatrix} t_{ij} & \Delta_i \\ \Delta_i^* & -t_{ji} \end{pmatrix}, \quad (32)$$

and eigenvalues $\{E_1, E_2, \dots, E_{2N}\}$. This procedure saves computational time. The eigenvalues are related by

$$E_{n+N} = -E_n. \quad (33)$$

For example, the anomalous correlator is given by

$$\langle c_{i\downarrow} c_{i\uparrow} \rangle_{2N} = \sum_{n=1}^{2N} \zeta_{n,i,1}^* \zeta_{n,i,0} f(E_n). \quad (34)$$

This is provably the same result as for the $4N$ case as can be seen by starting from the full expression

$$\langle c_{i\downarrow} c_{i\uparrow} \rangle_{4N} = \sum_{n=1}^{2N} \left(\check{\chi}_{n,i,1} (1 - f(E_n)) \check{\chi}_{n,i,2}^* + \check{\chi}_{n,i,3}^* f(E_n) \check{\chi}_{n,i,0} \right). \quad (35)$$

We then use what was shown above, namely if $(u_{ni}, 0, 0, v_{ni})$ is an eigenvector with eigenvalue E_n then $(0, u_{ni}, -v_{ni}, 0)$ is also an eigenvector $(\check{\chi}_{n+N,i})_i$ with eigenvalue E_n , to rewrite the sum into a sum over N positive eigenvalues via,

$$\begin{aligned} & \sum_{n=1}^N \left(\check{\chi}_{n,i,1} (1 - f(E_n)) \check{\chi}_{n,i,2}^* + \check{\chi}_{n,i,3}^* f(E_n) \check{\chi}_{n,i,0} \right. \\ & \left. + \check{\chi}_{n+N,i,1} (1 - f(E_n)) \check{\chi}_{n+N,i,2}^* + \check{\chi}_{n+N,i,3}^* f(E_n) \check{\chi}_{n+N,i,0} \right) \\ & = \sum_{n=1}^N \left(0 \cdot f(-E_n) \cdot 0 + u_{ni} f(E_n) v_{ni}^* \right. \\ & \quad \left. + u_{ni} f(-E_n) (-v_{ni}^*) + 0 \cdot f(E_n) \cdot 0 \right) \\ & = \sum_{n=1}^N u_{ni} f(E_n) v_{ni}^* - u_{ni} (1 - f(E_n)) v_{ni}^* \end{aligned} \quad (36)$$

Hence this expression reduces to the same as the $2N \times 2N$ one

$$\begin{aligned} \langle c_{i\downarrow} c_{i\uparrow} \rangle_{2N} & = \sum_{n=1}^{2N} \zeta_{n,i,1}^* \zeta_{n,i,0} f(E_n) \\ & = \sum_{n=1}^N \zeta_{n,i,1}^* f(E_n) \zeta_{n,i,0} + (-\zeta_{n,i,0}) \zeta_{n,i,1}^* f(-E_n) \\ & = \sum_{n=1}^N u_{ni} f(E_n) v_{ni}^* - u_{ni} (1 - f(E_n)) v_{ni}^*. \end{aligned} \quad (37)$$

B. RESULTS

B.1. Without phonons

The results of the time dynamics is shown for $\beta = 35$ in Fig. 1, where the plot shows the time evolution of the change in internal energy, $\mathcal{E}(\tau)$, and a site-averaged gap $\langle |\Delta| \rangle \equiv \sum_{i=1}^N \frac{1}{N} |\Delta_i|(\tau)$. The change in internal energy reaches a constant value some time after the laser pulse has subsided, which we refer to as \mathcal{E}_f . From top to bottom, the plots show the effects of increasing the energy absorbed from the laser pulse. The red horizontal line in the left column corresponds to the difference in internal energy between the superconducting state and the normal state before the pulse \mathcal{E}_{sc} . The blue line shows the change in internal energy $\mathcal{E}(\tau)$. The right column shows the melting of the superconductivity after the applied laser pulse. The red vertical line shows the time where the order parameter reaches its minimal value, corresponding to τ_m . The final absorbed energy initially increases with laser amplitude A_0 , with an accompanying increase in the melting time. This changes at a critical value of A_0 where the melting time starts decreasing rapidly. The value of \mathcal{E}_f where the maximum of τ_m occurs is temperature dependent, but it always occurs after \mathcal{E}_f surpasses \mathcal{E}_{sc} , yet before the value of \mathcal{E}_f which is sufficient to completely destroy the superconductivity and bring the order parameter to zero, \mathcal{E}_d .

The plot shows that the order parameter is gradually suppressed with increasing A_0 , until it finally changes sign around $A_0 \simeq 2.5$. This causes the absolute value to recover abruptly and results in a sharp reduction in melting time since the minimum value of $|\Delta|$ turns into a local maximum as Δ changes sign. The laser pulse thus causes an "overshoot" of the suppression of the order parameter beyond zero into negative values, whereas the U(1) symmetry of the superconducting condensate after the laser pulse has subsided renders $|\Delta|$ the physically meaningful quantity.

B.2. With phonons

We proceed to determine how the quench-induced dynamics of the superconducting order parameter is altered when there exists a coupling between the superconducting electron and an optical phonon mode ω . In this way, there can occur an energy exchange between the superconducting condensate and

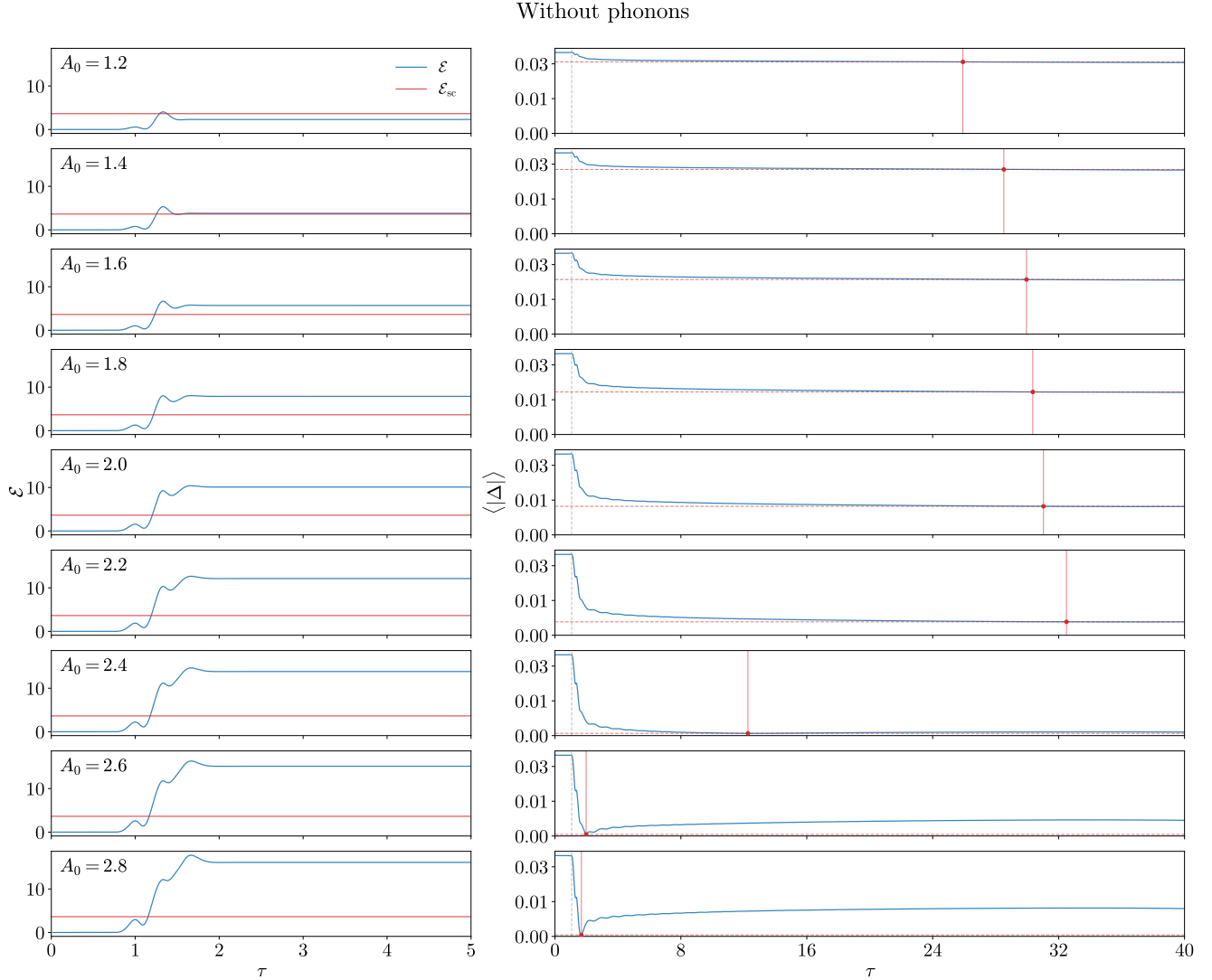


FIG. 1. Time dynamics of the absorbed internal energy and the order parameter averaged over all sites. The leftmost plots shows the absorbed internal energy \mathcal{E} in blue with gradually increasing laser amplitude A_0 , with the horizontal red line marking the difference in internal energy between the superconducting and normal state before the laser pulse is applied. The rightmost plots shows the time evolution of the site-averaged order parameter $\langle |\Delta| \rangle$ in blue. The red dashed horizontal line marks the minimal value that $\langle |\Delta| \rangle$ attains during the time-evolution, and the solid red vertical line and dot shows the time τ_m where this minimum value is attained. Parameters used are $U = -1, \beta = 35$ and $\omega = \gamma = 0$.

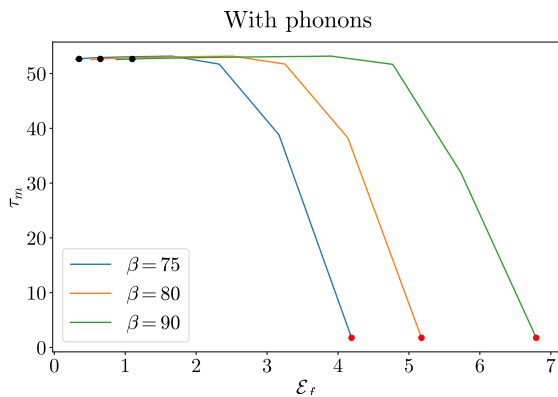


FIG. 2. Melting time τ_m versus absorbed internal energy for different choices of inverse temperature $\beta = 1/T$ with phonons. The black dots mark the melting time at the absorbed energy which equals the difference in internal energy of the superconducting and normal state at time zero, \mathcal{E}_{sc} . The red dots mark the melting time at the absorbed energy where the average of the order parameter goes to zero at some point during the time evolution. Parameters used are $N_x = 100$, $\omega = 0.3$, and $\gamma = 0.05$.

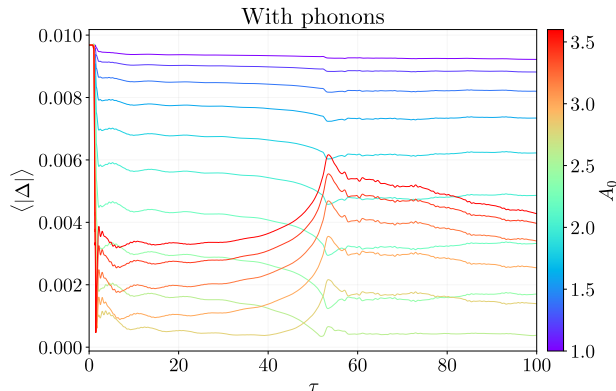


FIG. 3. Several time evolutions of the order parameter averaged over sites at inverse temperature $\beta = 75$ with different choices of the laser amplitude parameter A_0 . Parameters used are $N_x = 100$, $\omega = 0.3$ and $\gamma = 0.05$.

phonons in the system. Our self-consistent model thus captures (i) to what extent the phonons influence the melting of the superconducting state and (ii) how efficient the energy transfer between the superconducting condensate and the phonons is as a function of the injected energy through the laser-quench.

In Fig. 2 and Fig. 3, the melting time τ_m versus injected energy \mathcal{E}_f and rainbow plot of the time evolution of the site-averaged order parameter is shown. In Fig. 4, the absorbed energy as a function of time is shown next to the time evolution of the order parameter, marking the melting time and its relation to the ratio of \mathcal{E}_f and \mathcal{E}_{sc} . Notably, the absorbed energy for a given A_0 is much lower when coupling between electrons and phonons are present than when it is absent. The behavior of the melting time is qualitatively similar to the case without phonons, with the main difference being the absolute numbers and the behavior below \mathcal{E}_{sc} , where the melting time changes less before the rapid decrease. The latter behavior is more so explained by finite-size effects and quirks of the definition of melting time rather than a physical effect.

B.3. Periodic boundary conditions

The currents detailed in the main text depended on the hard boundary conditions of the lattice. If we implement periodic boundary conditions without also considering how the vector potential varies in space it is easy to see that the currents will vanish since there are no special sites where electrons can accumulate. With spatial variation though, for example a Gaussian modulation of the vector potential, currents are possible. The Gaussian modulation is given by modifying the vector potential according to

$$A(x, y, t) = A(t)e^{-\frac{(x-x_c)^2 + (y-y_c)^2}{2\sigma_g^2}}, \quad (38)$$

where x_c, y_c corresponds to the center of the lattice and σ_g decides the width of the modulation. See e.g. Fig. 5, though note that the Gaussian modulation is exaggerated compared to a realistic modulation in space to fit on the lattice and for illustrative purposes.

[1] P. C. Hohenberg and B. I. Halperin, Theory of dynamic critical phenomena, *Rev. Mod. Phys.* **49**, 435 (1977).

[2] N. Goldenfeld, *Lectures on Phase Transitions and the Renormalization Group* (CRC Press, Boca Raton, 1992).

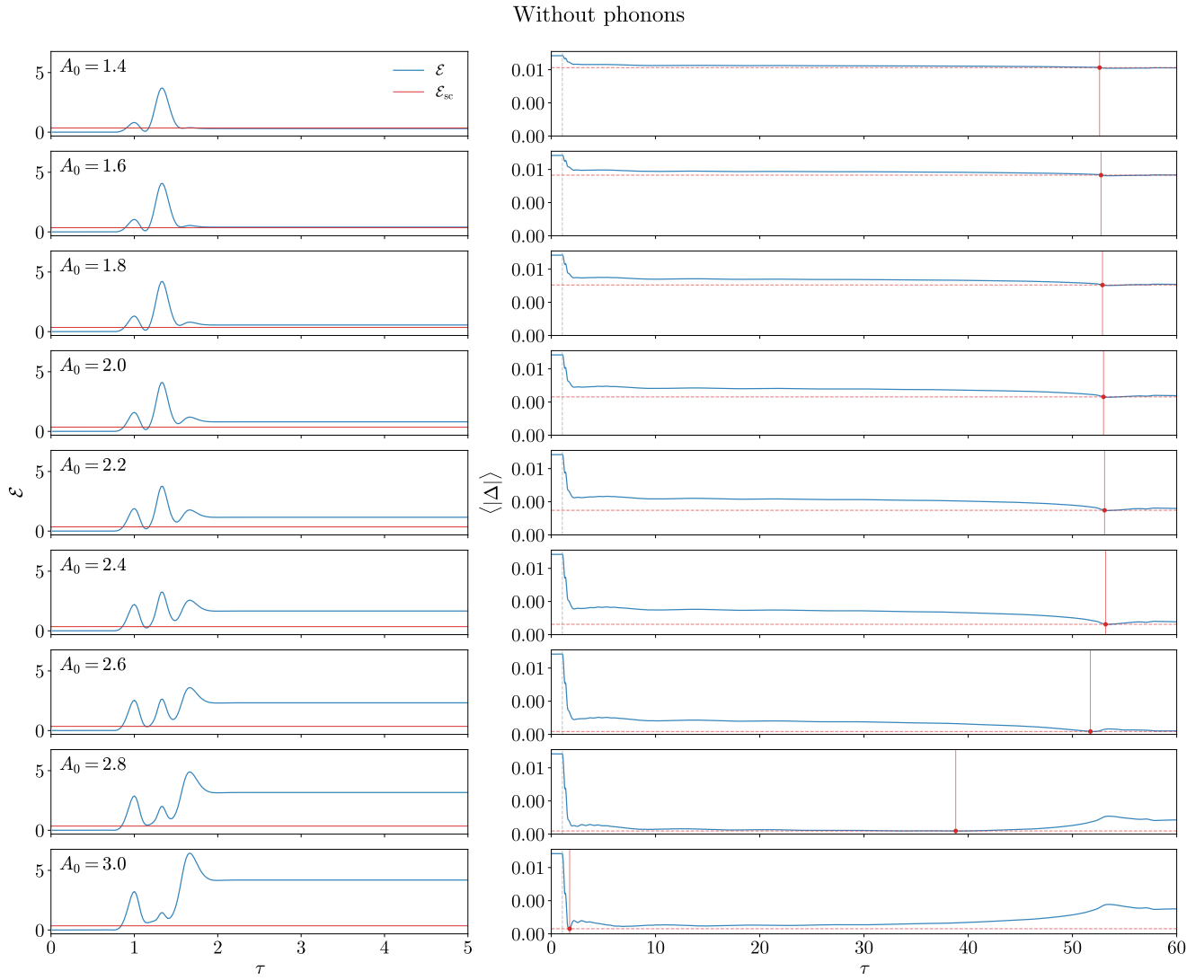


FIG. 4. Time dynamics of the absorbed internal energy and the order parameter averaged over all sites with phonons. The leftmost plots shows the absorbed internal energy \mathcal{E} in blue with gradually increasing laser amplitude A_0 , with the horizontal red line marking the difference in energy between the superconducting and normal state before the laser pulse is applied. The rightmost plots shows the time evolution of the site-averaged order parameter $\langle |\Delta| \rangle$ in blue. The red dashed horizontal line marks the minimal value that $\langle |\Delta| \rangle$ attains during the time-evolution, and the solid red vertical line and dot shows the time τ_m where this minimum value is attained. Parameters used are $N_x = 100$, $\omega = 0.3$, $\gamma = 0.05$ and $\beta = 75$.

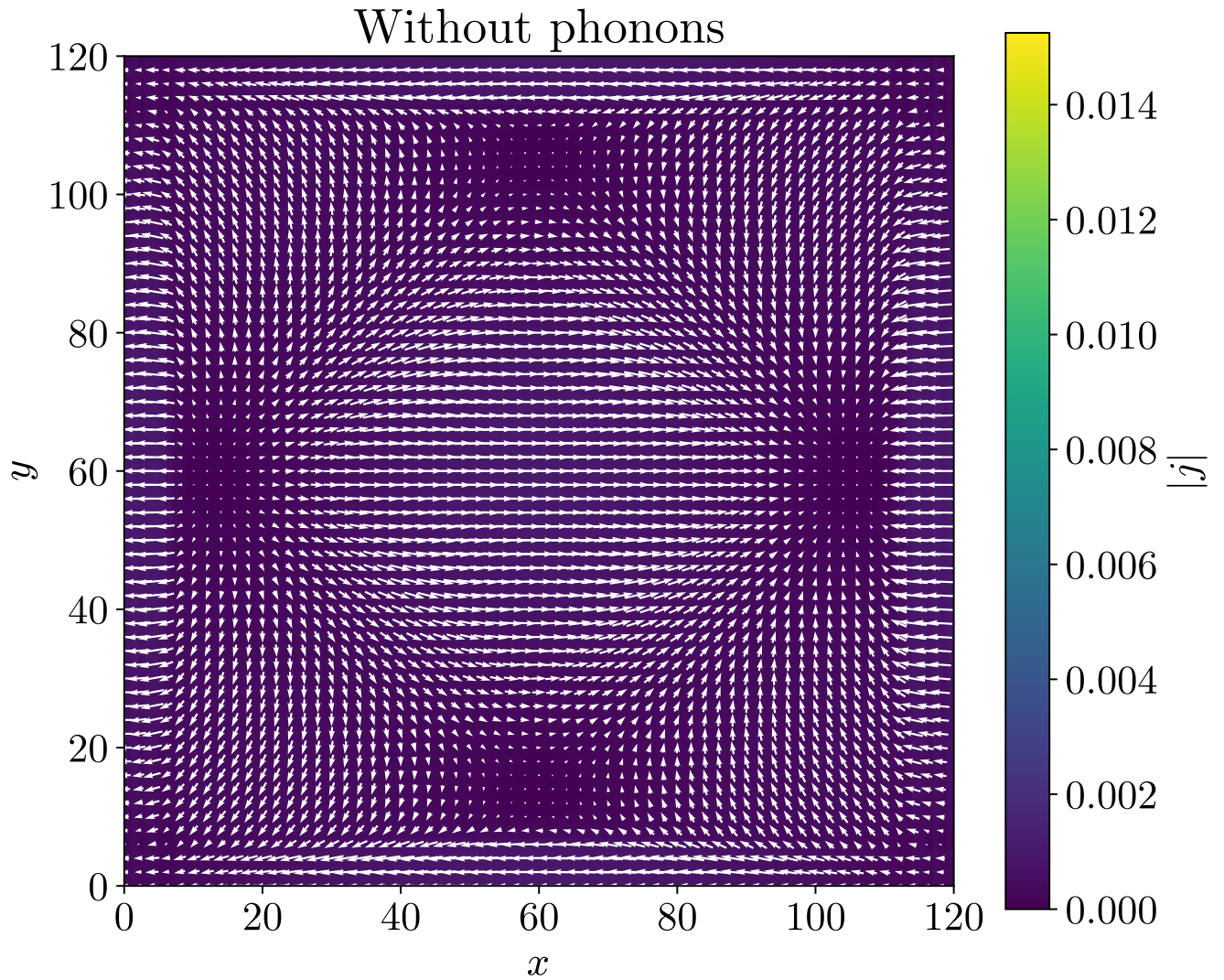


FIG. 5. Currents on a lattice at time $\tau = 5.5$ with periodic boundary conditions and a Gaussian modulated vector potential. The two magnitude-wavefronts on either end are both moving towards the center of the plot, but the currents are in the $-x$ -direction. Parameters used are $A_0 = 2.2$, $\beta = 10000$, $\mu = \omega = \gamma = 0$ and $\sigma_g = 60$.